Faraday Discussions

Cite this: DOI: 10.1039/d5fd00122f

ROYAL SOCIETY OF CHEMISTRY

PAPER

View Article Online
View Journal

Correlating binding energies of adsorbed CO and H on model surfaces with CO/H_2 selectivity from co-electrolysis of CO_2 and H_2O over copper–palladium bimetallic catalysts

Marcus Yu, †[a] Hong Zhang, †[b] William J. Wei, [a] Ping Liu [bc] and Jingguang G. Chen *[ac]

Received 21st November 2025, Accepted 22nd January 2026
DOI: 10.1039/d5fd00122f

Binding energies of adsorbed CO and H are key descriptors governing the activity and selectivity of the co-electrolysis of CO_2 and H_2O to produce syngas with desired CO/H_2 ratios. Palladium hydride (PdH), which forms *in situ* at negative overpotentials, has been identified as the active Pd phase for CO_2 reduction to syngas. Herein, binding energies of CO and H are determined using temperature programmed desorption (TPD) of CO and H_2 from Pd(111), PdH/Pd(111), and Cu/PdH/Pd(111) under ultra-high vacuum (UHV) conditions. TPD results reveal that desorption of H_2 from subsurface PdH occurs at 460 K, while desorption from surface PdH is more facile at 320 K. CO desorption temperatures shift 20 K lower on PdH/Pd(111) compared to on Pd(111). The presence of 0.7 ML Cu further increases the desorption temperature of H_2 by 30 K while simultaneously reducing CO desorption temperatures by 70 K. Density functional theory (DFT) calculations show that CO adsorption onto Pd sites is hindered on the 0.7 ML Cu/PdH/Pd(111) surface while the kinetic barrier for H_2 desorption is increased. The trends in the binding energies of CO and H on model surfaces are consistent with electrochemical measurements of CuPd powder catalysts in a membrane electrode assembly (MEA), where H_2 evolution is reduced while CO production is enhanced compared to unmodified Pd catalysts. Overall, the results from model surface studies (TPD and DFT) provide a prediction and explanation for the activity and CO/H_2 ratios observed in electrochemical experiments. This study also demonstrates that CuPd is a promising catalyst with reduced Pd-loading to produce CO-rich syngas.

[a]*Department of Chemical Engineering, Columbia University, New York, NY, 10027, USA. E-mail: jgchen@columbia.edu*

[b]*Department of Chemistry, State University of New York at Stony Brook, Stony Brook, NY 11794, USA*

[c]*Chemistry Division, Brookhaven National Laboratory, Upton, NY, 11973, USA*

† These authors contributed equally.

1 Introduction

CO_2 utilization is a promising method in tackling the rapid increase in atmospheric CO_2. Several popular strategies for CO_2 utilization are mineralization, syngas production, or as feedstocks for renewable fuels and fertilizer.[1–3] Among these, an increasingly attractive avenue for CO_2 utilization is the catalytical conversion of CO_2 into value-added forms of solid carbon, such as carbon nanofibers (CNFs) or graphene.[4–10] However, direct one-pot electrochemical conversion of CO_2 to CNFs is thermodynamically challenging and requires high temperatures (>700 °C).[11,12] Recently, Xie *et al.* showed that by coupling an electrochemical reactor for co-electrolysis of CO_2 and H_2O to syngas with a thermochemical reactor to convert syngas into CNFs, one can produce CNFs at a much lower temperature than was previously demonstrated with either thermochemical or electrochemical reactors alone.[4] They identified that the preferred pathway for forming CNFs was the Boudouard reaction ($2CO \rightarrow C(s) + CO_2$). Based on this, a higher CO production rate from co-electrolysis of CO_2 and H_2O should lead to more CNF formation by promoting the Boudouard reaction. An ideal electrocatalyst should be highly active and selective for the CO_2 reduction reaction (CO_2RR) to CO while also producing just enough H_2, from the competing hydrogen evolution reaction (HER) to keep the catalyst reduced in the thermochemical reactor. The development of an electrocatalyst that can produce syngas with tunable and desirable CO/H_2 ratios is thus necessary to optimize the production of CNFs from the tandem electrochemical–thermochemical reactor scheme.

There has been extensive research into CO_2RR to syngas, among which precious metals such as Ag, Au, and Pd have been identified as excellent catalysts with high activity, stability, and CO selectivity.[13–17] Pd stands out as an interesting CO_2RR catalyst due to its ability to dissociate H_2 and absorb atomic H to form a Pd hydride (PdH) phase.[18] At low overpotentials, Pd remains metallic and converts CO_2 to formate selectively.[19] However, as potentials are reduced to -0.2 V *vs.* RHE and below, absorption of atomic H into the bulk Pd lattice occurs, leading to lattice expansion and PdH formation, which coincides with a shift towards CO as the preferred CO_2RR product.[20]

To achieve higher CO/H_2 ratios, it is necessary to develop electrocatalysts with moderate CO binding energies. Pd-based catalysts typically suffer from CO poisoning that can reduce activity and selectivity for CO_2RR over HER.[21,22] As a result, much of the research in using Pd-based catalysts for CO_2RR has focused on reducing the CO binding energy to improve CO tolerance using various strategies such as alloying, doping, and facet control.[23–26] Several of these studies have identified that the formation of PdH is a key factor in enhancing the CO tolerance of Pd-based catalysts.[20,24,27] In the case of alloying, several studies have revealed that the addition of a secondary element such as C or Ag can inhibit PdH formation to control the degree of hydrogenation.[28–30] Regarding CO_2RR, Ag can be incorporated to hinder PdH formation, leading to enhanced formate selectively, which would be undesirable for the tandem reactor scheme to form CNFs.

In this paper, we experimentally determine activation energies of H_2 and CO desorption from a Pd(111) surface under ultra-high vacuum (UHV) with temperature programmed desorption (TPD). Following this, we demonstrate that we can

form a subsurface PdH/Pd(111) phase in UHV that is reproducible and stable. A separate, high temperature desorption peak for H_2 is observed on the PdH/Pd(111) surface that confirms the successful formation of a PdH phase. Additionally, we measure the effect of sub-monolayer (ML) Cu coverage on the PdH/Pd(111) surface on H_2 and CO desorption and reveal that at 0.7 ML, Cu acts to block available Pd sites and significantly hinders H_2 desorption while simultaneously reducing CO binding energy. DFT calculations indicate that Cu acts to block available Pd sites, preventing strong CO and H adsorption on Pd hollow sites. Cu significantly increases the diffusion barrier for both surface and subsurface H on PdH/Pd(111) to migrate and desorb, leading to the observed effects in the TPD experiments. We then correlate the results on model surfaces with electrochemical tests to show that trends in CO and H binding energies can be used to tune CO/H_2 ratios and guide CO_2RR electrocatalyst design.

2 Methods

2.1 Temperature programmed desorption

TPD experiments were carried out in a UHV chamber equipped with a Hiden HAL 3F-RC mass spectrometer for monitoring gas-phase species. The Pd(111) surface was first cleaned using Ne sputtering followed by annealing to 1000 K. Cu was deposited on the surface using physical vapor deposition from heating Cu wires wrapped around a Ta heating lead. Cu was removed and re-deposited before each experiment to ensure each surface was as consistent as possible and to minimize Cu migration into the Pd lattice. An Auger electron spectrometer (AES) was used to characterize the surface elemental composition following the quantification method developed by Cumpson *et al.*[31,32] A deposition curve was developed by monitoring the growth of the Cu (920 eV)/Pd(270 eV) ratio as a function of deposition time (Fig. S1). A sharp break at 8 minutes of deposition time indicated the completion of 1 ML Cu on Pd(111). Additionally, the linear fits suggested that Cu deposition followed the layer-by-layer growth mechanism on the Pd(111) surface. An AES peak ratio of 0.08 Cu (920 eV)/Pd(270 eV) was used to indicate the deposition of 1 ML of Cu on Pd.

H_2 and CO were dosed into the UHV chamber using a $\frac{1}{4}$ inch stainless steel tube attached to an external leak valve. Each leak valve was connected to a gas line that was evacuated with a turbopump. Immediately prior to the experiment, the gas-line was sealed from vacuum and filled with H_2 or CO respectively. Dosages were measured in Langmuir units (L, 1 L = 1×10^{-6} torr $\times$ s). The dosing temperature was 150 K for experiments on Pd(111), and 300 K for experiments on PdH/Pd(111) surfaces. Unless otherwise specified, the heating rate was 2 K s^{-1}.

2.2 Electrochemical experiments

Unless otherwise noted, all chemicals were obtained from Sigma Aldrich. Electrocatalysts with 10 wt% metal loading were synthesized following a previously reported procedure.[27] Gas diffusion electrodes were prepared using a standard ink formulation and airbrushing method.[4] A zero-gap MEA electrolyzer with a 5 cm^2 stainless-steel cathode flow field and titanium anode flow field separated by an anion exchange membrane (Sustainion X37-50 Grade RT, Dioxide Materials) was used to measure CO_2RR selectivity. The cathodic flow field was fed a mixture of 10 mL min^{-1} CO_2 and 2 mL min^{-1} Ar, while the anodic flow field was fed with 2

mL min^{-1} 50 mM $KHCO_3$. Electrochemical measurements were conducted using a BioLogic VSP potentiostat complemented with a Bio Logic VMP3B-20 (20 A/20 V) current booster. The cathode was pre-treated by conducting 20 cyclic voltammetry cycles between −0.2 V and −2.20 V (50 mV s^{-1}). To assess product selectivity, chronoamperometry was conducted at an applied potential of −3.0 V. The cathodic effluent was first passed through a water trap cooled with ice and then directed to the GC, an Agilent 7890B GC equipped with PLOTQ and MOLSIEVE columns and TCD and FID detectors, using an online connection. The CO/H_2 ratio was calculated from the molar fractions of CO and H_2 detected in the cathodic effluent.

2.3 DFT calculations

Spin-polarized DFT calculations were performed using the Vienna *Ab initio* Simulation Package (VASP).[33–35] The Perdew–Burke–Ernzerhof (PBE)[36] functional was used to describe electronic exchange and correlation. All structural optimizations were initialized using the Conjugate Gradient ionic relaxation algorithm[37] then converged with the RMM-DIIS ionic relaxation algorithm[38] with a plane wave cutoff energy of 400 eV. An electronic energy convergence criterion of 1×10^{-6} eV was applied, and ionic relaxation was performed until the Hellmann–Feynman forces on each atom were below 0.02 eV $Å^{-1}$.

A DFT optimized 1 : 1 β-PdH FCC unit cell with lattice constant of 4.140 Å was used to construct the PdH(111) surface.[39] The 4 × 4 PdH(111) surface consisted of four layers of Pd atoms, whereby the bottom two layers were restrained to represent the bulk structure underneath. The formation energy of the PdH(111) surface was found to be lower when terminated with H (Fig. S5). A 4 × 4 × 1 Monkhorst–Pack grid and first-order Methfessel–Paxton with a smearing width of 0.2 eV were used to integrate over the Brillouin zone. Periodic boundary conditions were applied to extend the surfaces infinitely. A vacuum spacing of 20 Å was added above the surface to ensure at least 15 Å of separation when Cu atoms or intermediate molecules were adsorbed, and dipole corrections were included along the vacuum direction.

Different models of Cu supported on PdH(111) with 0.3 ML and 0.7 ML coverage were used to find conformations with the lowest formation energy and minimized Cu–Cu bond strain with respect to the DFT optimized 3.629 Å Cu FCC crystal lattice. Distributed Cu atoms and 2D/3D islands of supported clusters were considered, and the formation energy of Cu_x/PdH(111) was calculated as:

$$\Delta E^0_{Cu_x/PdH(111)} = E_{Cu_x/PdH(111)} - E_{PdH(111)} - N \times E_{Cu} + M \times E_{H_2} \quad (1)$$

where $E_{Cu_x/PdH(111)} - E_{PdH(111)}$ represents the formation energy of Cu_x clusters based on the difference between the total energies of Cu_x/PdH(111) and clean PdH(111). $N \times E_{Cu}$ refers to the energy of N Cu atoms referenced to the Cu bulk chemical potential. The last term E_{H_2} describes the energy required to stabilize direct Cu–Pd bonds by removing H. Among the numerous Cu_x/PdH(111) clusters examined, 2D Cu_7 and Cu_{13} clusters were identified as the most stable configurations, corresponding to the 0.3 ML and 0.7 ML Cu used in H_2 and CO TPD experiments. Their relaxed Cu–Cu bonds closely resembled those of bulk Cu metal. (Fig. S6). The binding energies, B.E., of a given adsorbate molecule at 0 K were based on DFT calculated energies:

$$\text{B.E.} = E_{\text{adsorbate/surface}} - E_{\text{free molecule}} - E_{\text{clean surface}} \quad (2)$$

Under a specific temperature used in the TPD experiments, the free energy of adsorption $\Delta G_{(T)}$ was calculated as:

$$\Delta G_{(T)} = G_{\text{adsorbate/surface}} - E_{\text{clean surface}} - \mu_{\text{free molecule}} \quad (3)$$

where the total free energy of the surface with an adsorbate $G_{\text{adsorbate/surface}}$ is defined as the DFT calculated energy corrected with the zero-point energy (ZPE) and entropy at T (TS) from vibrational modes ν_i:

$$G_{\text{adsorbate/surface}} = E_{\text{adsorbate/surface}} + \text{ZPE} - TS \quad (4)$$

$$S = k_B \sum_i \left[\frac{\frac{h\nu_i}{k_B T}}{\exp\left(\frac{h\nu_i}{k_B T}\right) - 1} - \ln\left(1 - \exp\left(-\frac{h\nu_i}{k_B T}\right)\right) \right] \quad (5)$$

$$\text{ZPE} = \frac{1}{2}\sum_i h\nu_i \quad (6)$$

where the chemical potential of a free molecule $\mu_{\text{free molecule}}$ is expressed as:

$$E^0 + \text{ZPE} + \Delta H_{(T)} - TS \quad (7)$$

E^0 is the DFT calculated total energy of a gas phase molecule, ZPE and TS are obtained from the NIST Computational Chemistry Comparison and Benchmark Database (CCCBDB)[40] at the same level of theory used in our calculations, and the enthalpy change $\Delta H_{(T)}$ at temperature T is obtained from the NIST-JANAF thermodynamic table.[41]

The H diffusion rates, whether on the surface or from subsurface PdH, were derived from transition state theory:[42]

$$\text{Rate} = \frac{k_B T}{h} \exp\left(-\frac{(E_a)}{k_B T}\right) \times \theta \quad (8)$$

where k_B is the Boltzmann constant, T is the temperature in Kelvin, h is the Planck constant, and site density θ is the ratio between available site of diffusion with respect to the total number of Pd atoms on the surface. The activation barriers of diffusion E_a were obtained using the climbing image nudged elastic band (ciNEB) method,[43–46] with four intermediate images being manually generated between the optimized initial and final states of an H atom to minimize the travel distance and avoid overlap with other atoms along the path. The optimization was conducted by force-based RMM-DIIS algorithms and converged with <0.05 eV Å^{-1} of force acting on each ion. Saddle points were confirmed by vibrational frequency calculations that only applied to intermediate molecules and surface atoms that directly interacted with the adsorbate, with other atoms in the system being frozen.

3 Results and discussion

3.1 TPD results of H_2 and CO desorption from Pd(111) and PdH/Pd(111)

Binding energies of H and CO on Pd(111) were estimated from a series of TPD experiments with varying heating rates. Following H_2 or CO exposure, the Pd(111) surface was then heated at 0.5 K s^{-1}, 1 K s^{-1}, 2 K s^{-1} and 4 K s^{-1} and the peak

desorption temperatures (T_P) were measured (Fig. 1a and b). The linearized Redhead equation (eqn (9)), given below, was then used to determine the activation energy for desorption, E_d, based on the change in T_p as heating rates were varied (Fig. 1c and d).[47–49]

$$\frac{E_d}{RT_p} + \ln\frac{E_d}{k_0\theta_0{}^{n-1}} = -\ln\frac{\beta_h}{RT_p{}^2} \quad (9)$$

whereby R is the gas constant, k_0 is the pre-exponential factor, θ_0 is the initial surface coverage, n is the desorption order, and β_h is the heating rate. The slope of $\frac{1}{RT_p}$ *versus* $-\ln\frac{\beta_h}{RT_p{}^2}$ allows the determination of the activation energy for desorption E_d in the units of J mol^{-1}. By assuming that H_2 and CO have little to no activation barrier for adsorption, $-E_d$ could be approximated to be the binding energies of H and CO,[50,51] which were determined to be -83.6 kJ mol^{-1} and -161.7 kJ mol^{-1}, or -20.0 kcal mol^{-1} and -38.6 kcal mol^{-1}, respectively. These values were consistent with previously reported values by Ertl *et al.*, which were -20.8 kcal mol^{-1} for H and -34 kcal mol^{-1} for CO on Pd(111).[50,52]

Next, H_2 and CO were co-adsorbed onto the Pd(111) surface to determine if co-adsorption had any impact on the binding energies. H_2 desorption temperatures increased when CO was co-adsorbed on the surface (Fig. 2a). The peak temperature shifted from 318 K to 367 K and 385 K depending on the order of co-adsorption. Changing the order of co-adsorption (H_2 first or CO first) significantly impacted the amount of adsorbed H on the surface. Pre-adsorbed CO

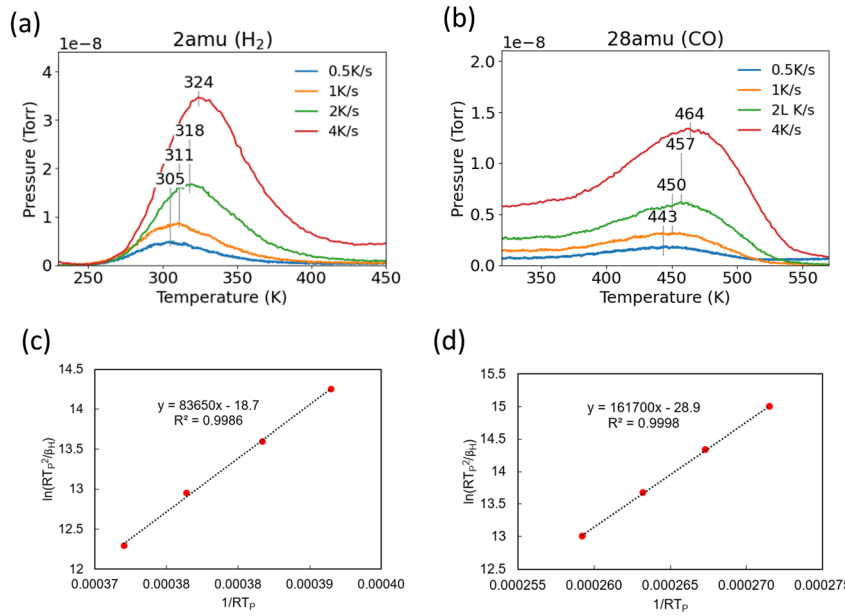

Fig. 1 TPD spectra after 10 L exposure of (a) H_2 or (b) CO were dosed onto the clean Pd(111) surface at 150 K. Heating rates were varied from 0.5 K s^{-1} to 4 K s^{-1}. Peak desorption temperatures of (c) H_2 and (d) CO at varying heating rates plotted using the linearized Redhead equation. The slope represents the activation energy for desorption in the unit of J mol^{-1}.

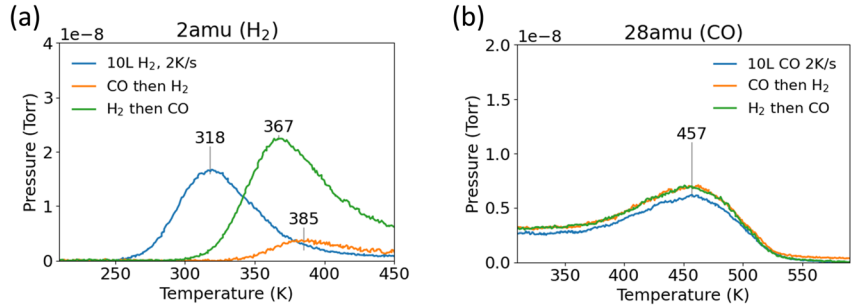

Fig. 2 TPD spectra of (a) H_2 and (b) CO following the co-adsorption of 10 L H_2 and 10 L CO on the Pd(111) surface. The adsorption order was alternated to observe the effect of pre-adsorbed H and CO on H_2 and CO binding and desorption.

blocked H_2 adsorption, leading to a diminished desorption peak area compared to when H_2 was adsorbed first. The desorption peak temperature was highest when CO was dosed first, which may have resulted from the lower coverage of adsorbed H. In comparison, the CO peak desorption temperature was not noticeably affected by the co-adsorption of surface H (Fig. 2b).

Previously, it had been determined that a PdH phase was likely the active phase during the electrocatalytic reduction of CO_2 to CO.[27] Therefore, it was desirable to create a PdH phase under UHV conditions on Pd(111) for further investigation on H_2 and CO adsorption. A PdH phase was successfully formed under UHV conditions by increasing the H_2 dosage to 600 L and holding the Pd(111) crystal at 300 K for several minutes to allow for H_2 dissociation and H migration into the subsurface region of Pd(111) (Fig. 3a). These experimental conditions were adapted from previous studies of H_2 adsorption on Pd(111).[50,53]

TPD experiments were then performed on the PdH/Pd(111) surface. Following this H_2 treatment, a second higher temperature H_2 desorption peak at 465 K appeared for PdH/Pd(111). Desorption of H_2 at temperatures above 450 K was characteristic of early transition metals, such as Ti, and was typically not observed in noble metals such as Pd or Pt.[54–56] Previous studies on Pd single crystal surfaces suggested that adsorption at liquid nitrogen temperatures (80 K) led to a saturation coverage of 1.5 ML H_2, with 1 ML on the surface (β-PdH), and another 0.5 ML existing in the subsurface layer (α-PdH).[53,57] Typically, this led to two separate desorption regimes, 150–200 K for α-PdH and 300–400 K for β-PdH. Desorption of H_2 at temperatures above 450 K suggested successful formation of a separate PdH phase in the Pd(111) subsurface region.

The amount of H_2 desorption from the surface PdH phase from 250–350 K after 600 L exposure was substantially reduced compared to H_2 desorption after 10 L exposure on clean Pd(111), despite being treated with 60 times more H_2. This suggested that the saturation coverage of surface H was reduced on the PdH/Pd(111) surface. The areas of the peaks were approximated using a simple Gaussian fitting (Fig. S2). The H_2 desorption peak area from surface PdH/Pd(111) was determined to be approximately half of the desorption peak area from Pd(111). If a saturation coverage of 1 ML of surface H was to be assumed on clean Pd(111), then the coverage of surface H was approximately 0.5 ML on PdH/Pd(111). Additional fitting showed

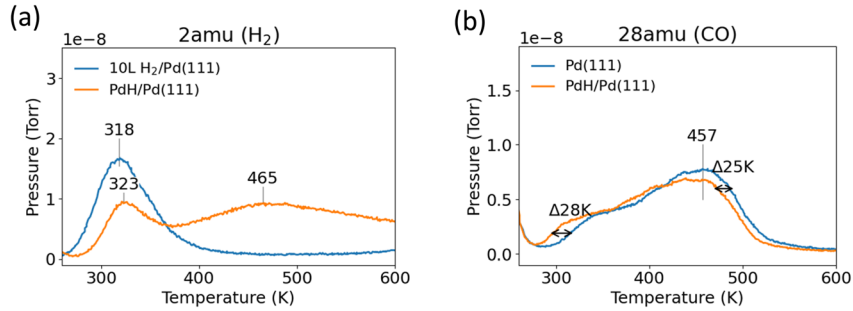

Fig. 3 (a) TPD spectra of H_2 after 10 L H_2 dosage at 150 K and 600 L H_2 dosage at 300 K without any CO co-adsorbed on Pd(111). (b) TPD spectra of CO after the co-adsorption of 10 L CO at 250 K onto the 10 L and 600 L H_2 pre-dosed surfaces. A broad H_2 desorption peak centered at 465 K indicates the formation of a stable, subsurface PdH/Pd(111) phase.

that the desorption area of H from subsurface PdH/Pd(111) above 320 K was equivalent to 2 ML, or twice that of the surface H saturation coverage on Pd(111).

The PdH/Pd(111) surface was cooled to 250 K and 10 L CO was adsorbed onto the surface to determine if PdH formation impacted CO binding energy (Fig. 3b). The peak shape for CO desorption was identical on both Pd(111) and PdH/Pd(111); however, the desorption temperature decreased by about 25 K on PdH/Pd(111). The desorption spectra of H_2 from the CO-covered PdH/Pd(111) surface is depicted separately in Fig. 4a. As expected, based on earlier results from the co-adsorption of CO on Pd(111) (Fig. 2), the surface H desorption peak shifted to about 50 K higher with the co-adsorption of CO (Fig. 4) onto PdH/Pd(111). However, CO adsorption on the surface does not seem to influence H desorption from PdH at 465 K. Lastly, AES showed no difference in the C peak before and after CO desorption, suggesting that CO desorbed reversibly on PdH/Pd(111).

3.2 TPD results for H_2 and CO desorption from Cu/PdH/Pd(111)

Following experiments on clean PdH/Pd(111), Cu was deposited onto the PdH/Pd(111) surface to determine its effect on H and CO binding energies. After exposing the Cu-modified PdH/Pd(111) surface to H_2 and CO, two H_2 desorption

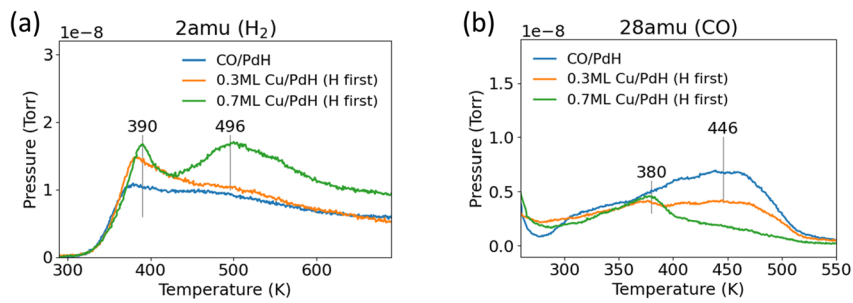

Fig. 4 TPD spectra of (a) H_2 and (b) CO desorption from CO-covered PdH/Pd(111) and CO-covered Cu-modified PdH/Pd(111) surfaces. The PdH/Pd(111) surface was prepared by 600 L H_2 dosage at 300 K.

peaks were still observed from the 0.7 ML Cu/PdH surface, suggesting that Cu on the prepared PdH/Pd(111) surface did not disrupt the existing PdH phase. Additionally, when the order of H_2 and Cu deposition was reversed, it was demonstrated that exposing a 0.7 ML Cu/Pd(111) surface to the 600 L H_2 treatment still led to successful PdH formation, indicating that a sub-ML Cu coverage did not hinder PdH formation (Fig. S3). After depositing 0.7 ML of Cu, the peak desorption temperature of surface H shifted slightly higher to 390 K from 370 K. More notably, the peak desorption temperature of subsurface PdH from the 0.7 ML Cu/PdH surface (Fig. 4a) shifted 30 K higher than that observed on CO-covered PdH/Pd(111) (Fig. 3). Additionally, the subsurface PdH peak became more intense and sharper, with a distinct separation from surface H desorption peak. At lower coverages of Cu (0.3 ML), there was an increase in the intensity and peak temperature of H_2 desorption from surface H without significant change in H_2 desorption from subsurface PdH. Meanwhile, the CO desorption peak temperature significantly decreased to 380 K from 457 K with 0.7 ML Cu coverage. At 0.3 ML Cu, the CO desorption spectra remained broad and did not result in a sharp peak like it did with 0.7 ML Cu. The CO desorption peak area also decreased by about 30% on 0.3 ML Cu/PdH compared to PdH/Pd(111), which suggested that at low coverages of Cu, CO preferentially bonded to available Pd sites. Overall, TPD results suggest that the presence of 0.7 ML Cu coverage on PdH/Pd(111) significantly reduced CO binding energy while simultaneously increasing H binding energy, which was an unexpected trend as H and CO binding energies often change in tandem instead of in opposite directions, as discussed in DFT calculations next.

3.3 DFT results

DFT calculations were carried out to gain a better understanding of the TPD results. Herein, a PdH film supported on Pd(111) was modeled by PdH(111) and two-dimensional Cu clusters adsorbed on PdH(111) were used to describe Cu-modified PdH/Pd(111) (Fig. S5 and S6). The results show that upon exposure to H_2, the dissociated hydrogen atom, H, prefers to adsorb at the 3-fold Pd hollow sites on the Pd-terminated PdH(111) surface (Fig. 5a). The surface thermodynamically prefers to be saturated by 1 ML H with an average binding energy (B.E.) of −0.27 eV per surface H atom, which is weaker than that on Pd(111) (B.E. = −0.66 eV per H).[58,59] The H monolayer is thermodynamically stable at 300 K and 400 K according to the calculated adsorption free energy ($\Delta G_{300K} = -0.06$ eV; $\Delta G_{400K} = -0.01$ eV) but becomes unstable when the temperature is raised to 500 K ($\Delta G_{500K} = 0.05$ eV). CO adsorption at 0.25 ML of coverage is also substantially weaker at the Pd hollow sites (B.E. = −1.36 eV) on Pd-terminated PdH(111) than that on Pd(111) (B.E. = −2.12 eV).[58] Compared to adsorbed H, adsorbed CO is much more stable on Pd-terminated PdH(111), remaining intact up to 500 K ($\Delta G_{300K} = -0.80$ eV; $\Delta G_{400K} = -0.63$ eV; $\Delta G_{500K} = -0.49$ eV). The CO saturation coverage is reached at 0.50 ML (average $\Delta G_{300K} = -0.75$ eV per CO; $\Delta G_{400K} = -0.57$ eV per CO; $\Delta G_{500K} = -0.47$ eV per CO). Upon exposure to a mixture of CO and H_2, 50% of Pd sites on Pd-terminated PdH(111) are preferentially saturated by CO, while the rest of the free Pd sites are likely occupied by H, featuring a stable surface configuration of 0.5 ML H + 0.5 ML CO (Fig. 5a).

The 0.3 ML Cu/PdH(111) was modeled by a Cu_7 cluster supported on Pd-terminated PdH(111) (Fig. 5b). CO preferentially occupies the 2-fold Cu bridge

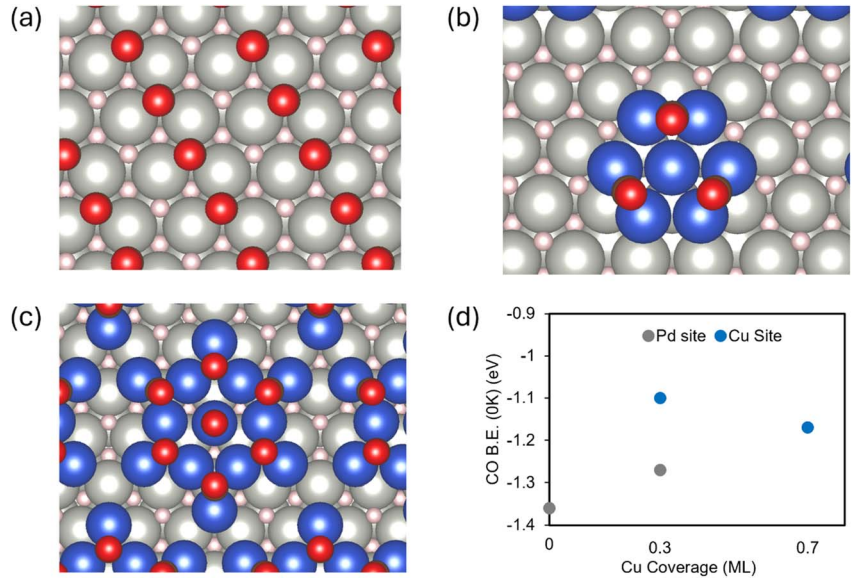

Fig. 5 DFT-optimized structures for (a) CO-saturated PdH(111); (b) 0.3 ML Cu/PdH(111); (c) 0.7 ML Cu/PdH(111). (d) DFT calculated B.E. of adsorbed CO at the most stable Cu or Pd site on each surface model. (Grey: Pd; blue: Cu; pink: H; red: CO).

sites at the edge of supported Cu clusters (B.E. = −1.10 eV per CO, Fig. S7a). It saturates at a coverage of 3 CO/Cu_7, which is stable up to 500 K (average ΔG_{300K} = −0.53 eV per CO; ΔG_{400K} = −0.37 eV per CO; ΔG_{500K} = −0.24 eV per CO, Fig. 5b). Additional CO adsorption is not preferred (ΔG_{300K} = 0.17 eV per CO; ΔG_{400K} = 0.31 eV per CO; ΔG_{500K} = 0.43 eV per CO). At a low Cu coverage of 0.3 ML, many Pd sites remain exposed at which CO can still adsorb, albeit with slightly weaker binding than that on PdH(111) (B.E. = −1.27 eV, Fig. S7a). Under co-adsorption of CO with H, atomic H does not prefer the Cu_7 cluster due to CO saturation, but instead prefers the exposed Pd hollow sites on the surface (Fig. 5b).

The increase in Cu coverage from 0.3 ML to 0.7 ML was described by cluster growth from Cu_7 to Cu_{13} on Pd-terminated PdH(111) (Fig. 5c). Wherein, the 3-fold Cu hollow sites at the edge are the most favorable for CO adsorption (B.E. = −1.17 eV, Fig. S7b), resulting in a saturation coverage of 7 CO/Cu_{13} with 6 CO at edge Cu hollow sites and 1 CO at the central Cu top site. This CO-saturated 0.7 ML Cu/PdH(111) configuration remains stable when the temperature is raised from 300 K to 500 K (ΔG_{300K} = −0.43 eV; ΔG_{400K} = −0.27 eV; ΔG_{500K} = −0.04 eV, Fig. 5c). At the Cu coverage of 0.7 ML, CO adsorbs only over Cu clusters whereas the very limited Pd sites are only accessible to adsorbed H (Fig. 5c). In this case, atomic H is highly coordinated by both Pd and Cu atoms at the Cu–PdH interface, which increases the stability of adsorbed H by 0.24 eV.

According to the DFT-calculated CO binding energies, increasing Cu coverage from 0 ML to 0.7 ML on PdH progressively weakens CO adsorption, driven primarily by changes in adsorption site preference from Pd hollow sites to Pd + Cu bridge sites and then to Cu only sites (Fig. 5d). This is consistent with the TPD observation of a decrease in CO desorption temperature with increasing Cu

coverage (Fig. 4). However, this is not the case for the desorption of atomic H as H_2. Specifically, the desorption of H is supposed to be promoted by the presence of CO saturation and Cu deposition on PdH(111), while TPD results show an increase in H_2 desorption temperature with the coverage of CO and Cu (Fig. 4a).

Unlike the molecular desorption of CO, H_2 desorption requires diffusion of adsorbed H and recombination of two neighboring H atoms. This process is not solely thermodynamically controlled but can also be strongly influenced by kinetics. The kinetic behaviors lie in H diffusion on the surface and from subsurface to surface. The adsorbed CO or deposited Cu atoms on the surface can potentially hinder the H migration along both paths. Indeed, the DFT-calculated diffusion barrier (E_a) for H migration increases when going from adjacent surface sites (Fig. 6a–d) to CO-saturated PdH and to CO-saturated Cu/PdH (Fig. 6a–c). Particularly, on 0.7 ML Cu/PdH, adsorbed H needs to diffuse along a long path that requires overcoming a high barrier of 0.42 eV (Fig. 6d). The E_a for H migration from the subsurface to the surface of Pd-terminated PdH(111) also shows the same trend, with E_a increasing from 0.08 eV on PdH to 0.24 eV on CO-saturated PdH and to 0.39 eV/(0.53 eV) on CO-saturated 0.3 ML/(0.7 ML Cu/PdH) (Fig. 6e–g). Overall, the DFT calculations well describe the peak shifts observed in the TPD results. Compared to Pd, the formation of PdH weakens CO and H adsorption, while Cu deposition progressively reduces CO binding but kinetically hinders H desorption by raising the energetic barrier for diffusion of adsorbed H.

3.4 Co-electrolysis of CO_2 and H_2O over PdH and CuPdH powder catalysts

To correlate trends in the binding energies of adsorbed CO and H over model surfaces with practical electrocatalysis, electrochemical studies of syngas production from co-electrolysis of CO_2 and H_2O were performed on Pd and CuPd powder catalysts. The CO/H_2 selectivity was evaluated at −3.0 V under enhanced CO_2 mass transport conditions by using a zero-gap MEA electrolyzer (Fig. 7a). Under CO_2 reduction conditions, the active phase of the catalyst is PdH.[27] For the

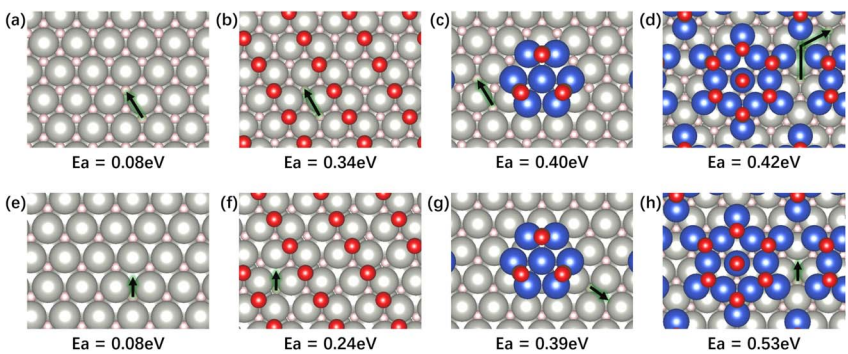

Fig. 6 Surface H diffusion path on (a) PdH(111); (b) 0.5 ML CO saturated PdH(111); (c) CO saturated 0.3 ML Cu/PdH; (d) CO saturated 0.7 ML Cu/PdH. Subsurface H diffusion to surface path on (e) PdH(111); (f) 0.5 ML CO saturated PdH(111); (g) CO saturated 0.3 ML Cu/PdH; (h) CO saturated 0.7 ML Cu/PdH; using Pd-terminated PdH(111) base. (The arrow represents the path of H diffusion). The corresponding barrier E_a is also included. (Grey: Pd; blue: Cu; pink: H; red: CO).

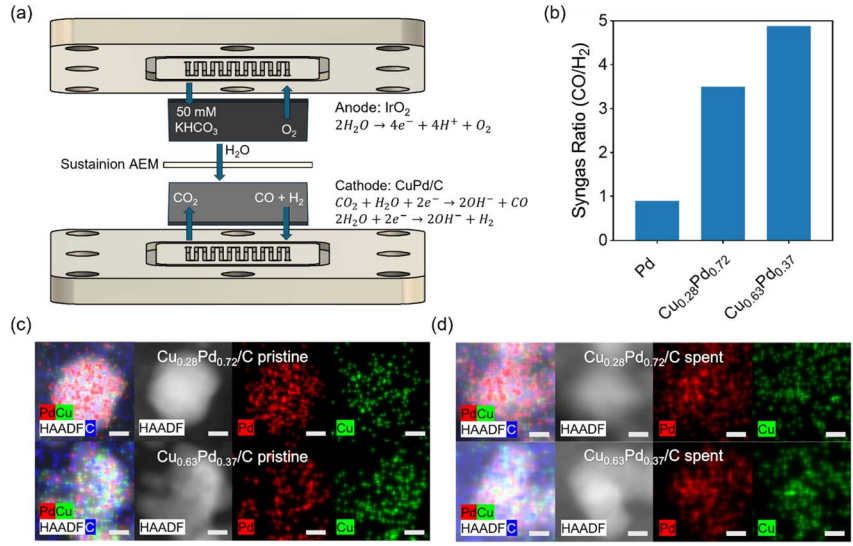

Fig. 7 (a) Schematic of the zero-gap MEA electrolyzer. (b) CO/H_2 ratios of syngas produced from the co-electrolysis of CO_2 and H_2O for Pd and CuPd powder catalysts with different Cu/Pd atomic ratios. HAADF-STEM imaging and STEM-EDS mapping of C, Pd, and Cu from the (c) pristine and (d) spent CuPd powder electrocatalysts. Scale bars are 5 nm.

pure Pd/C sample, the observed CO/H_2 ratio was 0.9 (Fig. 7b), owing to approximately equal molar production rates of CO and H_2. However, the CO/H_2 ratio increased to 3.5 and 4.9 as Cu content was subsequently increased in the $Cu_{0.28}Pd_{0.72}/C$ and $Cu_{0.63}Pd_{0.37}/C$ samples, respectively. Compared with previous literature on CO_2RR over CuPd electrocatalysts, the observed CO/H_2 ratio is relatively high, likely owing to differences in reactor configuration, electrolyte used, and electrocatalyst composition and morphology.[27,60] However, the trend in CO/H_2 is similar, directly resulting from an increase in selectivity towards CO_2RR to CO and a decrease in selectivity towards HER as Cu content was increased. The results from high-angle annular dark field (HAADF) imaging and energy-dispersive X-ray spectroscopy (EDS) mapping of the pristine (Fig. 7c) and spent (Fig. 7d) CuPd electrocatalysts suggest that Cu and Pd remain evenly distributed within nanoparticle clusters before and after CO_2RR. Overall, the powder catalyst study supports the TPD and DFT results in that the addition of Cu can be used to progressively weaken CO binding and hinder H_2 desorption, allowing one to control the CO/H_2 ratio in the syngas product by changing the atomic ratio of Cu/Pd in the bimetallic catalysts.

4 Conclusions

CO_2 utilization is a necessary technology for closing the carbon cycle and reducing CO_2 emissions. Pd catalysts are efficient for the co-electrolysis of CO_2 and H_2O to produce syngas; however, CO poisoning can represent a challenge for efficient and selective CO_2RR to CO. Within this work, experimental and computational studies on Cu/PdH model surfaces reveal key trends in modifying the binding energies of

adsorbed CO and H, which are then correlated with electrochemical measurements over the corresponding powder electrocatalysts. TPD results show that the formation of a PdH phase on the Pd(111) surface increases the barrier for H_2 desorption and simultaneously slightly reduces the CO desorption temperature. 0.7 ML Cu modification on the PdH/Pd(111) surface further reduces CO binding energy while hindering H_2 desorption. DFT results show that at 0.7 ML Cu coverage, there are no available Pd sites for CO to adsorb, forcing CO to adsorb onto Cu–Pd and Cu sites and consequently mitigating CO poisoning. Additionally, the Cu overlayer acts to increase diffusion barriers of adsorbed H, further hindering H_2 desorption. When the corresponding electrocatalysts are tested in an MEA electrolyzer, the CO/H_2 ratio increased from <1 on pure Pd to as high as 4.9 on CuPd bimetallic catalysts, indicating that alloying Pd with Cu can be used to control effluent CO/H_2 ratios while decreasing Pd loading in the electrocatalysts. Overall, results from the current study demonstrate the feasibility of using surface science studies to provide fundamental understanding and design strategies in practical catalysis over the corresponding powder catalysts.

Author contributions

MY: investigation, visualization, writing – original draft, writing – review & editing; HZ: investigation, visualization, writing – original draft, writing – review & editing; WW: investigation, visualization, writing – original draft, writing – review & editing; PL: supervision, funding acquisition, writing – review & editing; JGC: conceptualization, funding acquisition, project administration, resources, supervision, writing – review & editing.

Conflicts of interest

There are no conflicts to declare.

Data availability

Data for this article are available in an Open Science Framework repository. URL: https://osf.io/285yp/overview?view_only=9237a7f4d3874ac798f6308287836e6b.

Supplementary information (SI): raw mass spectra from TPD experiments, MEA product concentrations, dataset for all DFT structures and calculation settings. See DOI: https://doi.org/10.1039/d5fd00122f.

Acknowledgements

This work was financially supported by the United States Department of Energy, Office of Basic Energy Sciences, Catalysis Science Program (Grant No. DE-FG02-13ER16381). Marcus Yu acknowledges support by the National Science Foundation Graduate Research Fellowship under Grant No. DGE 2036197. DFT calculations in this work were performed using computational resources at Center for Functional Nanomaterials (CFN), and the Scientific Data and Computing Center, a component of the Computational Science Initiative, at Brookhaven National Laboratory under Contract No. DE-SC0012704, and at the National Energy Research Scientific Computing Center (NERSC), a DOE Office of Science User

Facility, supported by the DOE Office of Science under contract DE-AC02-05CH11231.

References

1 S. Zhang, M. Wu, Z. Qian, Q. Li, Y. Zhang and H. Zhou, *Fuel*, 2024, **357**, 130087.
2 J. Ding, R. Ye, Y. Fu, Y. He, Y. Wu, Y. Zhang, Q. Zhong, H. H. Kung and M. Fan, *Nat. Commun.*, 2023, **14**, 4586.
3 M. Liu and G. Gadikota, *Fuel*, 2020, **275**, 117887.
4 Z. Xie, E. Huang, S. Garg, S. Hwang, P. Liu and J. G. Chen, *Nat. Catal.*, 2024, **7**, 98–109.
5 Z. Xie, E. Huang, K. K. Turaczy, S. Garg, S. Hwang, P. R. Kasala, P. Liu and J. G. Chen, *Nat. Chem. Eng.*, 2025, **2**, 118–129.
6 X. Han, K. K. Ostrikov, J. Chen, Y. Zheng and X. Xu, *Energy Fuels*, 2023, **37**, 12665–12684.
7 X. Li, X. Wang, X. Hu, C. Xu, W. Shao and K. Wu, *J. Magnesium Alloys*, 2023, **11**, 1206–1212.
8 Z. Xie and J. G. Chen, *CCS Chem.*, 2024, **6**, 2855–2865.
9 Y. Yuan, B. Lamichhane, W. N. Porter, S. Hwang, L. Ma, D. Yang, A. Tayal, N. S. Marinkovic, S. Kattel and J. G. Chen, *Chem Catal.*, 2025, **5**, 101428.
10 Z. Xie and J. G. Chen, *CCS Chem.*, 2024, **6**, 2855–2865.
11 J. Ren, F.-F. Li, J. Lau, L. González-Urbina and S. Licht, *Nano Lett.*, 2015, **15**, 6142–6148.
12 S. Licht, A. Douglas, J. Ren, R. Carter, M. Lefler and C. L. Pint, *ACS Cent. Sci.*, 2016, **2**, 162–168.
13 S. Lu, Y. Shi, N. Meng, S. Lu, Y. Yu and B. Zhang, *Cell Rep. Phys. Sci.*, 2020, **1**, 100237.
14 T.-W. Jiang, K. Jiang and W.-B. Cai, *J. Mater. Chem. A*, 2024, **12**, 21515–21530.
15 R. T. Rashid, Y. Chen, X. Liu, F. A. Chowdhury, M. Liu, J. Song, Z. Mi and B. Zhou, *Proc. Natl. Acad. Sci. U. S. A.*, 2022, **119**, e2121174119.
16 B. M. Tackett, J. H. Lee and J. G. Chen, *Acc. Chem. Res.*, 2020, **53**, 1535–1544.
17 B. Chang, Z. Min, N. Liu, N. Wang, M. Fan, J. Fan and J. Wang, *Green Energy Environ.*, 2024, **9**, 1085–1100.
18 D. H. Everett and P. Nordon, *Proc. R. Soc. London, Ser. A*, 1997, **259**, 341–360.
19 A. M. Abdellah, F. Ismail, O. W. Siig, J. Yang, C. M. Andrei, L.-A. DiCecco, A. Rakhsha, K. E. Salem, K. Grandfield, N. Bassim, R. Black, G. Kastlunger, L. Soleymani and D. Higgins, *Nat. Commun.*, 2024, **15**, 938.
20 W. Sheng, S. Kattel, S. Yao, B. Yan, Z. Liang, C. J. Hawxhurst, Q. Wu and J. G. Chen, *Energy Environ. Sci.*, 2017, **10**, 1180–1185.
21 Y. Liu, D. Tian, A. N. Biswas, Z. Xie, S. Hwang, J. H. Lee, H. Meng and J. G. Chen, *Angew. Chem., Int. Ed.*, 2020, **59**, 11345–11348.
22 X. Chen, L. P. Granda-Marulanda, I. T. McCrum and M. T. M. Koper, *Nat. Commun.*, 2022, **13**, 38.
23 M. Zheng, X. Zhou, Y. Wang, G. Chen and M. Li, *Molecules*, 2023, **28**, 3169.
24 C. Ai, T. Vegge and H. A. Hansen, *ChemSusChem*, 2022, **15**, e202200008.
25 B. Xiong, J. Liu, Y. Yang, J. Ding and Z. Hua, *New J. Chem.*, 2022, **46**, 1203–1209.
26 H. Dong, L. Zhang, P. Yang, X. Chang, W. Zhu, X. Ren, Z.-J. Zhao and J. Gong, *Chem. Eng. Sci.*, 2019, **194**, 29–35.

27 J. H. Lee, S. Kattel, Z. Jiang, Z. Xie, S. Yao, B. M. Tackett, W. Xu, N. S. Marinkovic and J. G. Chen, *Nat. Commun.*, 2019, **10**, 3724.
28 M. W. Tew, M. Janousch, T. Huthwelker and J. A. van Bokhoven, *J. Catal.*, 2011, **283**, 45–54.
29 J. Chen, M. Aliasgar, Y. Zhao, F. B. Zamudio, L. Fan, J. Chen, J. Chen, X. Gu, J. Gao, S. M. Kozlov and L. Wang, *Nat. Commun.*, 2025, **16**, 10169.
30 K. Hyun, S. Yun and M. Choi, *ACS Catal.*, 2024, **14**, 2938–2948.
31 P. J. Cumpson and M. P. Seah, *Surf. Interface Anal.*, 1997, **25**, 430–446.
32 M. P. Humbert and J. G. Chen, *J. Catal.*, 2008, **257**, 297–306.
33 G. Kresse and J. Furthmüller, *Phys. Rev. B: Condens. Matter Mater. Phys.*, 1996, **54**, 11169–11186.
34 G. Kresse and D. Joubert, *Phys. Rev. B: Condens. Matter Mater. Phys.*, 1999, **59**, 1758–1775.
35 G. Kresse and J. Furthmüller, *Comput. Mater. Sci.*, 1996, **6**, 15–50.
36 J. P. Perdew, K. Burke and M. Ernzerhof, *Phys. Rev. Lett.*, 1996, **77**, 3865–3868.
37 W. H. Press, S. A. Teukolsky, W. T. Vetterling and B. P. Flannery, *Numerical Recipes: the Art of Scientific Computing*, Cambridge University Press, Cambridge, 3rd edn, 2007.
38 P. Pulay, *Chem. Phys. Lett.*, 1980, **73**, 393–398.
39 J. E. Schirber and B. Morosin, *Phys. Rev. B: Condens. Matter Mater. Phys.*, 1975, **12**, 117–118.
40 R. D. Johnson III, *NIST 101. Computational Chemistry Comparison and Benchmark Database*, https://www.nist.gov/publications/nist-101-computational-chemistry-comparison-and-benchmark-database, accessed October 14, 2025.
41 M. W. Chase, *NIST-JANAF Thermochemical Tables*, 4th edn, https://www.nist.gov/publications/nist-janaf-thermochemical-tables-4th-edition, accessed October 14, 2025.
42 R. A. Van Santen and J. W. Niemantsverdriet, *Chemical Kinetics and Catalysis*, Springer, US, Boston, MA, 1995.
43 G. Mills, H. Jónsson and G. K. Schenter, *Surf. Sci.*, 1995, **324**, 305–337.
44 H. Jónsson, G. Mills and K. W. Jacobsen, in *Classical and Quantum Dynamics in Condensed Phase Simulations*, World Scientific, 1998, pp. 385–404.
45 G. Henkelman and H. Jónsson, *J. Chem. Phys.*, 2000, **113**, 9978–9985.
46 G. Henkelman, B. P. Uberuaga and H. Jónsson, *J. Chem. Phys.*, 2000, **113**, 9901–9904.
47 G. Ertl, M. Neumann and K. M. Streit, *Surf. Sci.*, 1977, **64**, 393–410.
48 K. K. Turaczy, W. Liao, H. Mou, N. N. Nichols, P. Liu and J. G. Chen, *ACS Catal.*, 2023, **13**, 14268–14276.
49 A. Noordermeer, G. A. Kok and B. E. Nieuwenhuys, *Surf. Sci.*, 1986, **165**, 375–392.
50 H. Conrad, G. Ertl and E. E. Latta, *Surf. Sci.*, 1974, **41**, 435–446.
51 E. Ataman, M. P. Andersson, M. Ceccato, N. Bovet and S. L. S. Stipp, *J. Phys. Chem. C*, 2016, **120**, 16586–16596.
52 H. Conrad, G. Ertl, J. Koch and E. E. Latta, *Surf. Sci.*, 1974, **43**, 462–480.
53 G. E. Gdowski, T. E. Felter and R. H. Stulen, *Surf. Sci. Lett.*, 1987, **181**, L147–L155.
54 S. Suwarno and V. A. Yartys, *Bull. Chem. React. Eng. Catal.*, 2017, **12**, 312–317.
55 Y. Hirooka, M. Miyake and T. Sano, *J. Nucl. Mater.*, 1981, **96**, 227–232.

56 K. Christmann, G. Ertl and T. Pignet, *Surf. Sci.*, 1976, **54**, 365–392.
57 K. H. Rieder, M. Baumberger and W. Stocker, *Phys. Rev. Lett.*, 1983, **51**, 1799–1802.
58 H. Zhang and P. Liu, *Chem Catal.*, 2025, **5**, 101156.
59 H. Zhang, X. Wang and P. Liu, *Phys. Chem. Chem. Phys.*, 2022, **24**, 16997–17003.
60 J. Wang, G. Zhang, H. Liu, Z. Li, L. Wang, J. Tressel and S. Chen, *Sep. Purif. Technol.*, 2023, **320**, 124186.

